General model description of fission observables[a]

K.-H. SCHMIDT[b] and B. JURADO[c]
CENBG, CNRS/IN2P3, Chemin du Solarium B.P. 120, 33175 Gradignan, France

Abstract: Structural effects in fission-product yields and neutron data for a large number of fissioning nuclei between ^{220}Th and ^{262}Rf from spontaneous fission to 14-MeV-neutron-induced fission have been used to deduce information on the properties of the fissioning systems. Macroscopic properties are attributed to the compound nucleus, while fission channels are ascribed to shells in the nascent fragments. Using a recent general empirical description of the nuclear level density and assuming different characteristic time scales for the collective degrees of freedom of the fissioning system, a new fission model has been developed. The model combines the statistical concept of the scission-point model of Wilkins et al. with empirically determined properties of the potential-energy surface and some characteristic dynamical freeze-out times. The recently discovered energy-sorting mechanism in superfluid nuclear dynamics determines the sharing of intrinsic excitation energy at scission and the enhancement of even-odd structure in asymmetric splits. The model reproduces all measured fission yields and neutron data rather well with a unique set and a relatively small number of free parameters. Since the parameters of the model are closely related to physical properties of the systems, some interesting conclusions on the fission process can be deduced. Prospects for the predictive power of this approach for hitherto unknown fissioning systems are discussed.

Keywords: Fission-fragment yields; fission channels; fission dynamics; macroscopic-microscopic approach; separability principle; energy sorting; even-odd effect.

1. Introduction

Ordering schemes, systematics and semi-empirical models are powerful approaches for advancing our understanding of complex phenomena in nature. In nuclear fission great progress has been made by introducing the general concept of fission channels [1]. It established a link between the observed characteristics, e.g. in fission yields and kinetic energies, and the properties of the potential-energy surface of the fissioning system. However, it did not allow for quantitative predictions. The theoretical description of nuclear fission, in particular at low excitation energies with its rich manifestation of nuclear-structure phenomena is still a challenge. At present, one is restricted to purely empirical models (e.g. [2]) for a good quantitative description of the data.

In contrast, the theoretical description of atomic masses has reached a high degree of precision, and the complex phenomena behind the manifold global and structural effects are quantitatively rather well understood. The data are very well reproduced by models based on the macroscopic-microscopic approach, while fully microscopic models are supposed to be more realistic for nuclei close to the drip lines.

In the present work we try to profit from the powerful concepts and methods successfully used in mass models in order to establish a model of the fission process. We make use of several well

a Final report of a research project in the frame of EFNUDAT, October 2010
b E-mail: k.h.schmidt@gsi.de
c E-mail: jurado@cenbg.in2p3.fr

known and a few newly developed concepts to develop a description for fission-fragment distributions and the properties of prompt neutrons, which reproduces the experimental data with high precision and which is expected to have a high predictive power for systems that have not been measured and that are not accessible to experiment.

Empirical descriptions of fission-fragment distributions reveal similarities and systematic trends when the nuclear composition or the excitation energy of the fissioning system is varied. One prominent example is the variation of the relative weights and of the properties of the fission channels. Theoretical descriptions, based on the characteristics of the potential-energy landscape on the fission path with the macroscopic-microscopic approach [1, [3], [4]] and fully microscopic calculations [[5]] provide some basic understanding of these regularities. However, the ability of theory for quantitative predictions is limited, and the precision of purely theoretical models cannot yet compete with the one obtained with empirical models [2]. But also the applicability of empirical models is rather restricted due to their poor predictive power.

2. Reminder on methods and concepts used in mass models

Atomic mass models [[6]] span the range from local formulas [[7]], directly based on measured mass values, to microscopic models based on effective nucleon-nucleon interactions. However, intermediate approaches proved to be the most successful ones for a long period. A rather good description of the binding energy of atomic nuclei has been proposed by C. F. von Weizsaecker already in 1935. It relies on the analogy of an atomic nucleus with an electrically charged drop of a classical liquid. By additionally considering the Fermionic nature of the nucleons by the asymmetry term, the liquid-drop model reproduces the nuclear binding energies with a precision of about 1 per cent. In the macroscopic-microscopic approach, structural effects due to shell effects and pairing correlations are calculated separately by the Strutinsky method [[8]] and a suited pairing model [[9]], and then added to the value obtained by the liquid-drop model. The liquid-drop model still gives a very good estimation of the global behaviour of nuclear binding for nuclei not too close to the drip lines, which is at present hardly reached by microscopic models that rely on the interactions of nucleons governed by an effective nuclear force.

A systematic analysis of empirical data and a careful comparison with global models, like the liquid-drop model, have proven to be very useful in establishing evidence for phenomena, which go beyond the basic description. Exceptionally high binding of nuclei along "magic numbers" due to shell effects [[10], [11]], even-odd structure due to pairing correlations and the manifestation of the congruence energy [[12]] were recognized by systematic deviations from the liquid-drop predictions. The role and the magnitude of the spin-orbit force have been deduced [[13], [14]], and the appearance of new magic numbers far from stability has been evidenced [[15]]. The comparison of nuclear properties with a global background acts as a magnifying glass on structural effects and new phenomena and, thus, forms the important counterpart to microscopic models, which try to model the complex phenomena on a more fundamental level. One should not forget that also microscopic nuclear models remain phenomenological [[16]], since the effective force is adjusted to reproduce best the body of experimental data.

3. Concept of a general fission model

The experimental information available for low-energy fission of a specific nucleus is by far more rich than just one numerical value like its atomic mass: These are the many individual nuclide yields, the kinetic energies of the fission fragments, the prompt neutron yields and neutron energies, to mention the most prominent ones, only. Moreover, the fission observables are the result of a complex dynamical process, while the ground state of a nucleus is the energy of an equilibrium state. Thus, the modeling of the fission process appears to be much more difficult.

In the same manner as refs. [[17], [18]], we consider that the features of the fission yields are essentially

determined by the sum of the macroscopic potential, given by the liquid drop model (LDM), and shell effects. In the excitation-energy domain of interest for this work, the yields are generally interpreted according to the concept of independent fission modes or channels [1]. The different fission modes correspond to specific valleys in the potential-energy landscape. One distinguishes between three main modes the 'super long' (SL), 'standard 1' (S1) and 'standard 2' (S2). The SL mode is characterised by symmetric yields and low total kinetic energy TKE, which can be explained by a strong deformation of both fission fragments at the scission configuration. The standard modes S1 and S2 present asymmetric mass distributions with average masses of the heavy fragments located near 134 and 140, respectively. The asymmetric modes S1 and S2 present higher TKE than the SL mode, the TKE of S1 being again 10 to 12 MeV higher than that of S2. This can be understood by a scission configuration with one spherical heavy fragment and a deformed light fragment for S1, and a configuration with two moderately deformed fragments for S2. While the SL channel is associated to the LD macroscopic potential, the two asymmetric standard modes are generally thought to be linked with shells in the heavy fission fragments at $N = 82$ and $Z = 50$ (spherical shell) for S1 and $N \approx 88$ (deformed shell) for S2 [19]. There are indications for another, more asymmetric mode, often denoted as super-asymmetric mode [20 ,21]. In the following, we will use the term 'standard 3' (S3).

Any fission model needs to follow the dynamic evolution of the fissioning system up to scission. The number of protons and neutrons in the two fragments, their kinetic energies, the available energies above their respective ground states as well as their angular momenta are decided or can uniquely be deduced from the scission configuration. However, it is not justified to assume statistical equilibrium at scission as it was done by Wilkins et al. [19], because a considerable inertia may prevent the system to adjust instantaneously to the bottom of the potential-energy valley on the fission path. One may assume that there is a dynamical freeze-out somewhere before reaching scission, which is specific to the different collective variables. The mass asymmetry degree of freedom is characterized by a rather early freeze-out due to its large inertia [22], while the *N/Z* degree of freedom is decided later, because the mass transport and consequently the inertia associated with the charge polarization is much lower [23]. Thus, there is no single, well defined configuration, where the statistical-model assumption seems to be justified.

Due to this difficulty and the unavoidable uncertainty of a theoretical fully dynamic calculation, we decided to extract the relevant information from the available experimental data directly. The measured characteristics of the distributions in the different variables contain the required information in the most precise and realistic way. However, it is not clear, whether this approach is feasible, because we should establish this empirical information for each fissioning system independently. Thus, this approach would be equivalent to a purely empirical model with a specific parameter set for each fissioning system. One cannot expect a high predictive power for unmeasured systems from this kind of approach.

We apply the separability principle [24] to solve this problem. Indeed, two-centre shell-model calculations revealed that the shell effects of the fissioning system already immediately beyond the outer saddle are very similar to the sum of the shells in the two nascent fragments [25]. The combination of this finding with the macroscopic-microscopic approach leads to a very important conclusion: The shell effects on the fission path are associated to the nascent fragments. Essentially the same shell effects are present if the same fragments are formed in different fissioning systems. Thus, the full body of experimental data on fission-fragment properties can be used to deduce the relevant information on shell effects on the fission path, which are the same for all fissioning systems. Only the macroscopic potential on the fission path is specific to the fissioning system. Thus, we expect that the separability principle of microscopic effects, which are associated to the nascent fragments, and of macroscopic effects, which are specific to the fissioning system, makes our approach feasible and gives it a high predictive power.

The final aim of this work is to develop a code for predicting the fission-fragment yields of all the nuclei from polonium to fermium and beyond for excitation energies E^* ranging from 0 to 15 MeV.

The code should be easily implemented in reactor simulation codes for nuclear-waste transmutation and reactor safety. Recently, the results of a coordinated research project from the IAEA aiming at the development of systematics and nuclear models for the prediction of minor actinides fission yields up to 150 MeV neutron energy have been presented [26]. This report contains various systematics based on fits of several Gaussians to experimental mass yields. These systematics give very accurate results for regions located very close to the nuclei used to extract the parameters of the fit. Although our code contains a few parameter dependences that have a pure experimental origin, it is mainly based on well founded physical arguments. Therefore, we expect the predictive power of our code to be better than pure systematics in regions where the amount of data is very poor as is the case for minor actinides.

4. Formulation of the model

Fission is a dynamical process where the collective degrees of freedom evolve under the influence of the available number of states above the potential-energy surface, friction and inertia. In this work we consider the following collective variables: the quadrupole deformation of the nascent fragments β_1 and β_2 together with the effective distance between the surfaces of the fragments d, which stands for the length of the neck, the mass asymmetry, and the ratio N/Z of each fission fragment. The saddle point is a particular point on the way to fission with limited phase space that justifies the application of the statistical model to estimate the population of the transition states at the fission barrier [27]. Collective variables, which develop slowly compared to the saddle-to-scission time keep a memory of a configuration close to saddle. This is expected for the mass-asymmetry degree of freedom, mainly due to the associated large inertia [22]. On the other hand, the N/Z degree of freedom [23] and the deformation [28] have a small inertia and are essentially determined by the available number of states at scission. We consider that the probability for each fission channel is determined by integrals over the level density up to the available energy at the saddle point. This is valid under the assumption of independent fission channels where the potential-energy valleys associated to the different fission modes are well separated when moving from saddle to scission, and the leakage from one mode to the other is excluded.

The determination of the full potential landscape via theoretical calculations is rather complex and, in spite of the progress made, these calculations do not reproduce the observed facts with good precision. Therefore, in our case we extract this information from the available experimental data.

A basic ingredient of the model is the curvature of the macroscopic potential in mass-asymmetry on the fission path at freeze out of the asymmetry degree of freedom [29]. This value determines the width of the mass-symmetric fission channel and, even more importantly, the relative strengths of the asymmetric fission channels. The shell effects, which are responsible for the asymmetric fission valley, are fully effective, if they appear close to symmetry. This is the case for the heavier actinides. In contrast, the influence of these shell effects is weakened in the lighter actinides, where these shells appear at larger asymmetry. This interplay of the macroscopic potential and the shell effects determines the transition from single-humped mass distributions to double-humped distributions around $A = 226$ [30].

We present here in some detail the analysis of the mean position of the heavy component of the fission-fragment distribution as an example of the ingredients of the fission model. Fig. 1 shows the systems, for which mass or nuclear-charge distributions have been measured, on a chart of the nuclides. The position of the heavy component shows a regular pattern, but the previous assumption [31, 32] that the position is constant in mass appears to be strongly violated. It is rather the proton number, which is fixed at $Z = 54$. For this finding, the long isotopic chains studied in an experiment in inverse kinematics play a decisive role [30]. Thus, we implement in our model that the freeze out of the mass-asymmetry degree of freedom leads to a nearly constant position in the atomic number of the heavy fragment. A similar kind of analysis has been made for the different fission channels, which are considered in the model [33]. Further details are given in section 4.2.

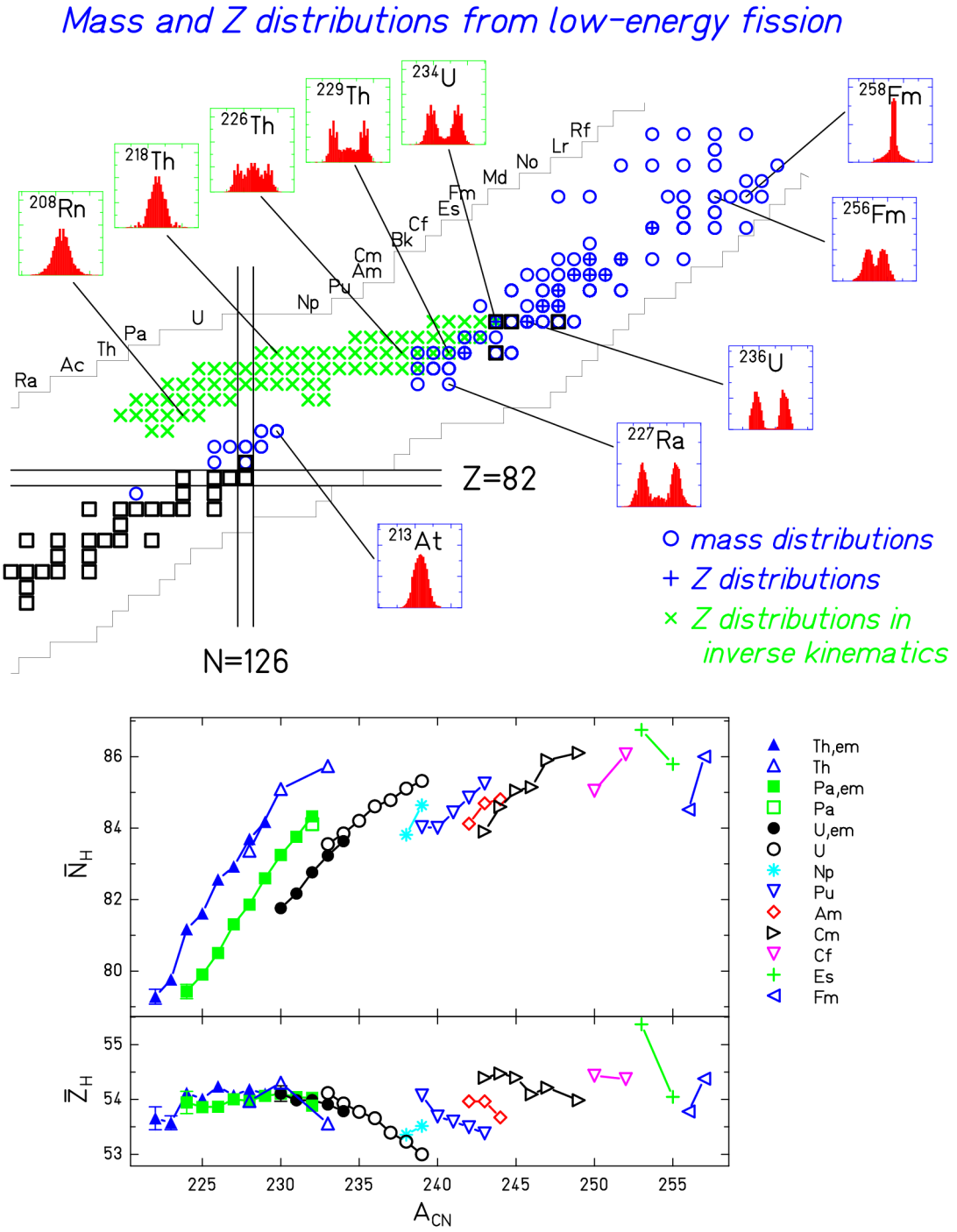

Figure 1: Upper part: Overview on the systems, for which mass or nuclear-charge distributions have been measured. The green crosses denote the systems which have been measured in inverse kinematics after electromagnetic excitation [30]. Lower part: The mean position of the asymmetric component in the heavy group in neutron number and in atomic number. Obviously, the traditional statement that the heavy component is constant at A = 140 must be revised by this analysis on a finer scale: The position of the asymmetric component is nearly constant at Z = 54, while the position in neutron or mass number varies by about 7 units.

Some other structural effects, which were deduced from experimental data, are the *Z*-dependent deformation parameters of the fragments and the mean value and the width of the charge polarisation at scission. The fractions of the energy release from saddle to scission which end up in intrinsic and collective excitations have been fixed, too. Another important ingredient of the model is the energy-sorting mechanism [34], which is responsible for the division of the intrinsic excitation energy at scission and for the creation of an even-odd effect in asymmetric mass splits [35].

Finally, the model includes an evaporation code, which determines the prompt neutron yields from the two fragments as well as their kinetic energies. Gamma competition is considered; it smoothes out the consequences of the even-odd fluctuations of the neutron-separation energies.

4.1 Level densities

Contrary to most of the work done in fission, we use the constant-temperature level density [36]:

$$\varrho(E^*) \propto \frac{1}{T} e^{\frac{E^*}{T}} \tag{1}$$

where T is the nuclear temperature defined as the inverse of the logarithmic derivation of the level density with respect to excitation energy. The available experimental data on level densities reveal an approximate constant-temperature behaviour up to at least $E^* \approx$ 6-7 MeV [37]. It seems that the melting of Cooper pairs as a function of excitation energy causes an almost linear increase of the effective number of nuclear degrees of freedom, which leads to a constant temperature in the superfluid regime [38]. Moreover, it was found recently that the constant-temperature description remains valid up to 20 MeV for medium mass nuclei [39]. In nature, this constant temperature behaviour appears in solid-liquid and liquid-gas phase transitions. Note that the often used Fermi-Gas level density [40] represents the asymptotic behaviour of the level density at high E^*, where the temperature of the system increases in proportion to $\sqrt{E^*}$. Hence, this description is not well adapted to the E^* regime considered here.

4.2 Mass asymmetry

As said above, in our model the mass yields are determined near the outer fission saddle. To define the nuclear potential in mass asymmetry we assume that the macroscopic potential at saddle follows a parabola whose curvature C_{LD} is given by $C_{LD} = 8K / A_{CN}^2$, where K is a parameter that depends on the fissility of the fissioning nucleus Z_{CN}^2 / A_{CN}. This dependence has been experimentally studied and parameterised in refs. [29, 41] on the basis of measured mass distributions. According to this parameterisation, the curvature C_{LD} increases linearly with fissility up to $Z_{CN}^2 / A_{CN} = 35$ and then decreases. However, in our study we observed that this decrease fails in describing the transition from mass-asymmetric fission of the heavier actinides to mass-symmetric fission of neutron-deficient light actinides. We have found that the latter transition can only be reproduced if the linear increase is maintained for $Z_{CN}^2 / A_{CN} > 35$.

Also in theory, the variation of the stiffness with fissility is a subject of debate: While some models predict a decrease around $Z_{CN}^2 / A_{CN} = 30$ [41], a monotonic increase of the stiffness with fissility was predicted by Nix [42]. Our result seems to support Nix' model. We may suppose that some contribution from quasi-fission or fast fission could be responsible for the increasing widths of the mass distributions of the heavy actinides, which entered into the parameterisation of refs. [43, 29]. This problem certainly needs more careful investigation.

We consider only the shell effects that lead to the three asymmetric modes S1, S2, and S3. These shell effects are represented by parabolas whose curvatures and depths are free parameters that are adjusted to the available experimental data. As said above, one generally assumes that the modes S1

and S2 are mainly conditioned by shells in neutron number. Actually, S1 is also the result of the proton shell Z=50, although most calculations show that this shell is weaker than the shell at N=82. However, very surprisingly, experimental yields show that the mean position of the heavy fragment associated to channel S1 remains very much stable at $<Z^h_{S1}>=52.5$, which implies strong systematic variations in neutron number. Similarly, the mean position of channel S2 stays rather constant at $<Z^h_{S2}>=55$, while the average neutron number varies. This observation has been established for a broad range of fissioning nuclei between Ac and Cf [33].

When studying this issue in more detail, considering an even larger number of nuclei, we have found a slight dependence of $<Z^h_{S1}>$ and $<Z^h_{S2}>$ on the mass of the fissioning system.

The essentially constant position of the heavy- fragment groups of the S1 and S2 fission channels in Z is a crucial ingredient of our model. The theoretical explanation is not clear. Pashkevich deduced a stabilisation around the 'magic' proton number Z = 54 at large deformation in his shell-model calculations [44]. However, a deformed proton shell in this region is not found by other authors, see e.g. refs. [19, 45].

The appearance of the S3 fission channel is most clearly seen by a pronounced shoulder on the wings of the mass distribution in spontaneous fission of ^{252}Cf, for which very accurate measurements exist. However, due to its low relative yield and the limited precision of the experimental data for many other systems, the parameters of this channel are rather uncertain. In addition, it was not possible to reproduce the observed variation of its strength by attributing the S3 channel to a single shell, e.g. at N = 52, as suggested in ref. [20]. Tentatively, the S3 fission channel has been parameterised as the combined influence of a shell at Z = 59.5 in the heavy fragment and at Z = 37 in the light fragment.

4.3 Fission-fragment deformation

The deformation of the fragments at scission is strongly favoured by the mutual Coulomb repulsion of the nascent fragments that induces a considerable elongation of their shapes. The deformation induced in the two nascent fragments can be considered as a superposition of a macroscopic trend given by respective Coulomb repulsion and the restoring force of the surface tension of the LDM, which favours a large prolate deformation around β = 0.5 [19], and a structural influence due to shell effects. As said previously, different fission modes correspond to substantially different deformations at scission. The energy stored in deformation is transformed into E^* of the fragments when they snap back to their ground state deformation after separation. The number of neutrons evaporated by each fission fragment is thus very sensitive to the deformation at scission.

Theoretical arguments on the deformation of the fragments at scission can be deduced from shell-model calculations [19, 45]. These calculations reveal a very characteristic and systematic feature of shell effects at large prolate deformation: There is a strong correlation between the particle number (neutrons or protons) and an increasing deformation. This feature had already been associated earlier [19] with the variation of the neutron yields as a function of fragment mass. These curves present a saw-tooth-like behaviour with a minimum for the heavy spherical fragment associated to mode S1 and a maximum number of neutrons for the complementary fragment. We considered this feature by assuming linear dependences of β_1 and β_2 with Z_1 and Z_2 , respectively, which are obtained from experimental data on prompt neutron yields as a function of the fragment mass $\nu(A)$. The tip distance d is a free parameter whose value is fixed with the help of $\nu(A)$ data and total kinetic energy (TKE) measurements.

4.4 Charge polarisation

Given a scission configuration of two emerging fragments A_1 and A_2 with deformations β_1 and β_2 with a tip distance d, we calculated the macroscopic shape of the potential at scission as a function

of the *N/Z* degree of freedom by taking into account the Coulomb repulsion between the two nascent fragments and the LD potential for each fission fragment. The result is a parabola with a minimum for *N/Z* that deviates from the value of *N/Z* of the fissioning nucleus, that is, from the unchanged charge density (UCD) assumption. The deviation with respect to the UCD hypothesis is called charge polarisation.

Polarisation is expected to be enhanced by the combined influence of the shells $N = 82$ and $Z = 50$ of the S1 mode. Directly measured polarisation data can be used to deduce the influence of the S1 shell on the *N/Z* degree of freedom. Post-neutron yields, however, need to be corrected for prompt neutron emission. Besides, the influence of Coulomb and surface energy on polarisation depends strongly on β_1 and β_2 and on the tip distance d. As mentioned in the previous section, experimental data on $\nu(A)$ give considerable information on these deformation parameters.

4.5 Variances

Once the parabolic shape of the potential for a given degree of freedom is established, the probability distribution for the degree of freedom can be determined by considering the nucleus like an harmonic oscillator in contact with a heat bath of temperature T. This leads to a Gaussian distribution with variance:

$$\sigma^2 = \frac{\hbar\omega}{2C}\coth\left(\frac{\hbar\omega}{2T}\right) \tag{2}$$

where ω is the frequency of the harmonic-oscillator potential and C is the stiffness of the potential. At low temperature $T \ll \hbar\omega$, expression (2) leads to the width of the distribution corresponding to the quantal zero-point motion: $\sigma^2 = \hbar\omega/(2C)$. At high temperature $T \gg \hbar\omega$, eq. (2) gives $\sigma^2 = T/(2C)$.

However, in the constant-temperature regime, eq. (2) leads to a constant width, and this is in contradiction with the observation that the width of the fission-fragment mass distributions increases with increasing E^* [46, 47]. The reason for this discrepancy is that eq. (2) has been obtained by integrating the probability distribution associated to each harmonic oscillator state weighted with the occupation probability of each state as given by a Boltzmann distribution. The integration extends up to infinite E^*, which means that there is a certain probability to put a very large E^* in the degree of freedom. This canonical assumption is valid in classical mechanics for a gas but it is not valid for a nucleus where the E^* is limited. In the case of a nucleus, the integral is truncated at the E^* of the system, and this leads to an increase of the width with E^* even in the constant-temperature regime.

There is another reason why the widths of the asymmetric fission channels grow with increasing excitation energy: Since in these cases the restoring force is caused by shell effects, the washing out of shell effects in the level density reduces the restoring force towards the potential minimum and, thus, leads to an increase of the mass width.

In our model we have used the experimental data of [29] to determine the coefficients of the linear relation between σ^2 and E^*. For the dependence of σ^2 with the mass of the fissioning nucleus for each fission mode we have used the data from C. Boeckstiegel et al. [33]. A recent systematic study of the width and the mean value of the *N/Z* degree of freedom in fission has been performed in ref. [48].

4.6 Tunneling

If the initial excitation energy is close to the fission barrier or even lower, tunneling becomes important. The relative population of the different fission channels is decided by the tunneling through the outer barrier, where the entrance points of the fission valleys in the potential energy of the fissioning system are located. Note that the tunneling through the inner barrier(s) influences the

yields of all fission channels in the same way. With the constant-temperature level-density description (1) and the Hill-Wheeler expression for the tunneling, the yields of the different fission channels are obtained by the following integral:

$$Y_i \propto \int_0^\infty \frac{1}{T} e^{\frac{\epsilon}{T}} \frac{1}{1+e^{2\pi\frac{(\epsilon+B_i-E^*)}{\hbar\omega_B}}} d\epsilon \tag{3}$$

It is assumed that the available energy E^* - B_i above the barrier is shared between intrinsic excitation energy ε and kinetic energy E^* - B_i - ε. Formally, negative kinetic-energy values correspond to tunneling. B_i are the heights of the saddle points associated with the different fission channels. The temperature T is defined by the level-density description (see above). We found that the value of the barrier-transmission parameter $\hbar\omega/(2\pi)=0.3\,\mathrm{MeV}$ for all fission channels and all fissioning systems reproduces the data rather well. It should be stressed that this value should not be compared with the slope of fission excitation functions, which results from the tunneling through the whole barrier. Small variations of the barrier-transmission parameter according to the reduced mass and the influence of shell effects improve the agreement with experimental data.

4.7 Reduction of the S1 fission channel at low excitation energies

The division of the fission flux between the S1 and the S2 fission channels at energies around the fission barrier shows a particularity, which has been carefully investigated by Brosa et al. [49]. While for nuclei with $A < 236$ the relative yield of the S1 grows with energy, the slope is reversed for heavier nuclei, see figure 4 of ref. [49]. Brosa et al. distinguish between "increasers" and "decreasers". This transition is rather localized in a narrow mass range $234 \leq A \leq 238$.

In the frame of our model, we observed that the increasers are characterised by lower excitation energies at scission than the decreasers. A systematic view in the yields supports the role of the excitation energy at scission rather than the mass of the fissioning system as the key parameter for the division of the fission flux between the S1 and the S2 fission channels. This way, both the transition from the increasers to the decreasers as well as the energy dependences of the different systems are attributed to a common origin. Thus, the observed features could be explained if one assumes a mechanism, which suppresses the yield of the S1 fission channel at low excitation energies. This mechanism should have the behaviour of a switch, which alternates between two different states.

We propose the following tentative explanation: In accordance with theoretical studies of the potential-energy landscape [1], we assume that the division between the S1 and the S2 fission channels takes place somewhere between saddle and scission, where *on the average* already part of the potential-energy gain is transformed into intrinsic excitation energy due to dissipation. At this stage, also other properties, e.g. the pairing correlations, might already be specific to the nascent fragments. If the average dissipated energy is small, there is a high probability that the division between the S1 and the S2 fission channels is taken when the intrinsic excitation energy of the nucleus is zero. If compared to the energies of the excited states, the state with $E^* = 0$ is lowered by the pairing gap. Since the pairing gap depends on the single-particle level density at the Fermi level, it is particularly small in the heavy nascent fragment corresponding to the S1 fission channel, which is attributed to the strong spherical $Z = 50$ and $Z = 82$ shells.

When considering this scenario with a reduced pairing gap for the S1 fission channel, the division between the S1 and S2 fission channels is drastically improved. The parameters have been adjusted to the data.

4.8 Joined fission valleys

The transition from low-TKE asymmetric fission in ^{256}Fm to high-TKE symmetric fission in ^{258}Fm

and other nuclei in this region has been attributed to the combined influence of the ^{132}Sn shell in both nascent fragments on the potential-energy surface [50]. In the frame of the GEF code, a quantitative description of this phenomenon had to be found. In fact, it is not sufficient to consider the lowering of the potential at the bottom of the fission valley corresponding to the superposition of the shells in the two nascent fragments. Already when the ridge between the two S1 fission valleys corresponding to the proximity of the ^{132}Sn shell closure in the two nascent fragments becomes transparent for mass-asymmetric oscillations, the zero-point energy decreases. This leads to a considerable decrease of the effective depth of the combined fission valley. This feature is also able to explain why the symmetric fission appears so suddenly when only one or two neutrons are added to the fissioning nucleus.

4.9 Excitation energy of the fission fragments

We assume that near the scission configuration the two nascent fragments have already acquired their individual properties concerning shell effects [25, 51, 52] and pairing correlations [53] and can be treated as two well defined nuclei set in thermal contact through the neck. We will now consider how the total excitation energy TXE is divided between the two nascent fragments. Following the transition-state approach of Bohr and Wheeler [27], all the available E^* above the barrier height is assumed to be thermalised, that means it is equally distributed between all degrees of freedom. The difference in potential energy between saddle and scission [54] may feed some amount of pre-scission kinetic energy in fission direction, excitations of normal collective modes and additional intrinsic excitations. We may distinguish three classes of energy, which add up to the final TXE of the fission fragments at scission:

(i) Collective excitations stored in normal modes.

(ii) Intrinsic excitations by single-particle or quasi-particle excitations.

(iii) Deformation energy.

The division of collective excitations among the two fragments is intimately related to the nature of the specific collective mode considered. We have assumed that this energy is equally distributed among the two fission fragments. Direct information on the contribution of collective energy to the E^* of the heavy fission fragment can be obtained from the number of neutrons emitted by fragments of mass A = 130, since this mass corresponds mainly to spherical fission fragments from the S1 channel, and, thus, the contribution from deformation energy is small. The division of intrinsic excitations can be derived when thermal equilibrium is assumed among the intrinsic degrees of freedom in each fragment. Considerations on the applicability of thermodynamical concepts to the configuration of two nuclei in thermal contact can be found elsewhere [55]. As said above, the nuclear level density at low E^* is very well described by the constant-temperature formula of eq. (1). Egidy et al. obtained the following dependence of the parameter T of eq. (1) from the nucleus mass number A and from shell effects S from a fit to available data on level densities [37]:

$$T = \frac{1}{A^{1/3}}(17.45 - 0.51\,S + 0.051\,S^2) \tag{4}$$

This leads to a very interesting situation for the two nascent fragments at the scission-point configuration: The level density of each fragment is represented by the constant-temperature formula (1) with a specific value of T for each fragment. As a consequence, there is no solution for the division of the intrinsic E^* with $T_1 = T_2$. As long as the fragment with the higher temperature is not completely cold, its E^* is transferred to the fragment with the lower temperature. That means, a process of energy sorting takes place where all E^* accumulates in the fragment with the lower temperature, while the other fragment looses its entire E^* [34]. According to formula (4), the heavy fragment generally has the lower T and thus attracts all the E^*. However, due to the influence of shell corrections on T, this trend may be reversed if the heavy fragment is stabilised by a strong shell effect. This may be expected in the S1 fission channel, which is characterised by the formation

of a heavy fragment close to the doubly magic ^{132}Sn. The flow of E^* from the hot fragment (the fragment with the higher T) to the cold fragment (the fragment with the lower T) can be seen as a way for the entire system made of the two nascent fragments in contact to maximise the number of occupied states. The number of available states of the light nucleus or closed-shell nucleus is small compared to that of the complementary fragment. Therefore, the situation in which the light nucleus or the closed-shell nucleus has part of the E^* leads to a smaller number of occupied states than the situation in which the entire E^* is transferred to the heavy or the non-closed shell nucleus which offers considerably more available states.

4.10 Even-odd effect in fission-fragment yields

A review on the even-odd structures in the fission-fragment yields reveals regular global features as a function of Coulomb parameter and asymmetry \[[56]]. These features are very well reproduced by a dynamical model, which considers the formation of even-even nuclides, generally in the light fragment, as the end process of the energy-sorting mechanism. Details are given in a dedicated article [35]. Even-odd staggering in symmetric splits is described by the model presented in [[57]].

4.11 Evaporation

For the E^* domain considered in this work, neutron evaporation from saddle to scission can be excluded. Scission neutrons are still a subject of debate. Therefore, we only consider neutron emission from the fission fragments. Neutron evaporation has been modelled taking into account the neutron binding energy of each fission fragment. The neutron kinetic energy is sampled from a Maxwell distribution with the temperature T as given by eq. (4). The latter distribution is truncated in order to satisfy energy conservation. Gamma competition is schematically considered by applying systematically higher effective neutron-separation energies in the case of even-even, even-odd, and odd-even daughter nuclei. This modification tends to flatten out even-odd structures, which are created in the evaporation process.

5. Parameters

The most important parameters of the model, which are directly adjusted to the fission data, are listed in table 1. These 13 parameters, together with the few mentioned already in this text, are most decisive for the results. The description of additional parameters, which determine some finer details of the model, would go beyond the scope of this article. They may directly be extracted from the code [[58]].

The values of most parameters appear to be reasonable in view of theoretical expectations. Some give new insight into fission and ask for a better theoretical understanding, like the constant positions of the fission valleys in Z. A few inconsistencies appear or re-appear, e.g. the insufficient charge polarization obtained by the scission-point model (see below). They suggest further studies.

Table 1: The values of the most important parameters of the fission model. (The dissipated energy is given as the fraction of the potential-energy release from saddle to scission [54]. The S3 fission channel appears only with full strength when it coincides with $Z = 37$ in the light fragment. See [27] for details of the description of the even-odd effect.)

Fission channel	**Z**	**Depth**	**curvature**
Standard 1	52.5	-3.1 MeV	0.4 MeV / c^2
Standard 2	55	-4.0 MeV	0.13 MeV / c^2
Standard 3	59.5	-6.6 MeV	0.15 MeV / c^2
Dissipated energy	**fraction**		
Normal modes	0.35		
Intrinsic	0.45%		
Neck distance			
d	1 fm		
Charge polarisation			
Additional shift	0.37 units		
Even-odd effect			
Threshold	$(T_1\text{-}T_2)/E^* = 0.035$		
Standard deviation	0.07 (T_1 - T_2)		

6. Comparison with data

Figures 2 to 9 show a comprehensive comparison of the present version of the model with evaluated and measured mass distributions for spontaneous, thermal-neutron-induced, fast-neutron-induced, and 14.6-MeV-neutron-induced fission. In addition to the values of post-neutron yields from the ENDF B VII evaluated data files, mostly based on radiochemical measurements, some additional data from kinematical measurements for spontaneous fission have been added.

Figures 10 and 11 demonstrate the reproduction of the energy dependence of the mass distribution in comparison with experimental data for neutron-induced fission of ^{238}U.

The gradual transition from symmetric to asymmetric fission in the region of the light actinides around $A = 226$ is shown in figures 12 and 13.

The mass distributions give only a partial view on the predictions of the model, which also calculates full nuclide distributions before and after emission of prompt neutrons. Figure 14 and 15 compare the measured and the calculated charge polarization and the widths of the isobaric charge distributions for the systems ^{235}U(n_{th},f) and ^{249}Cf(n_{th},f).

The average number of prompt neutrons as a function of fragment mass is shown in figures 16 and 17 for neutron-induced fission of ^{237}Np and spontaneous fission of ^{252}Cf.

In general, the agreement of the model with the empirical data is rather good. The remaining discrepancies may be attributed to (i) insufficient adjustment of the model parameters, (ii) shortcomings of the model approach, and (iii) problems in the measured or evaluated data. It is difficult to say, how much the model could be improved by a better choice of the parameter values. Indeed the complexity of the problem prevented us to develop an automatic fit procedure. Thus the adjustment was performed with an “eye fit”. The quality of the model also depends on the amount

and the diversity of the data, which were chosen for comparison out of the huge body and the immense complexity of the relevant empirical information.

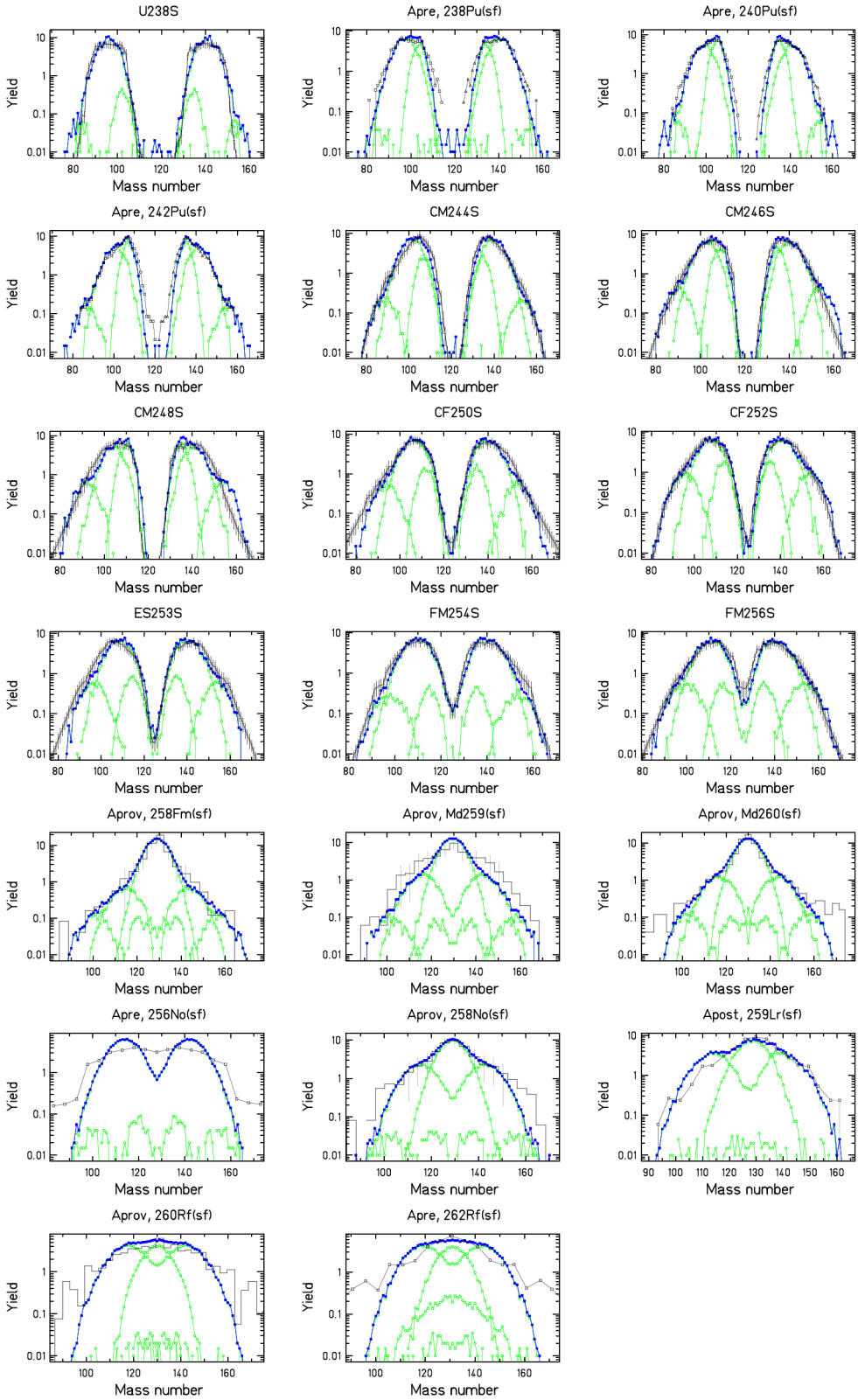

Figure 2: Comparison experimental post-neutron (Apost), pre-neutron (Apre) and provisional (Aprov) mass distributions as well as evaluated post-neutron mass distributions from spontaneous fission [[59], [60], [61]] (black crosses, histograms or open squares) with calculated post-neutron respectively pre-neutron mass distributions [58] (full blue symbols). The contributions of the different fission channels are shown in addition (open green symbols). The fissioning nuclei are indicated.

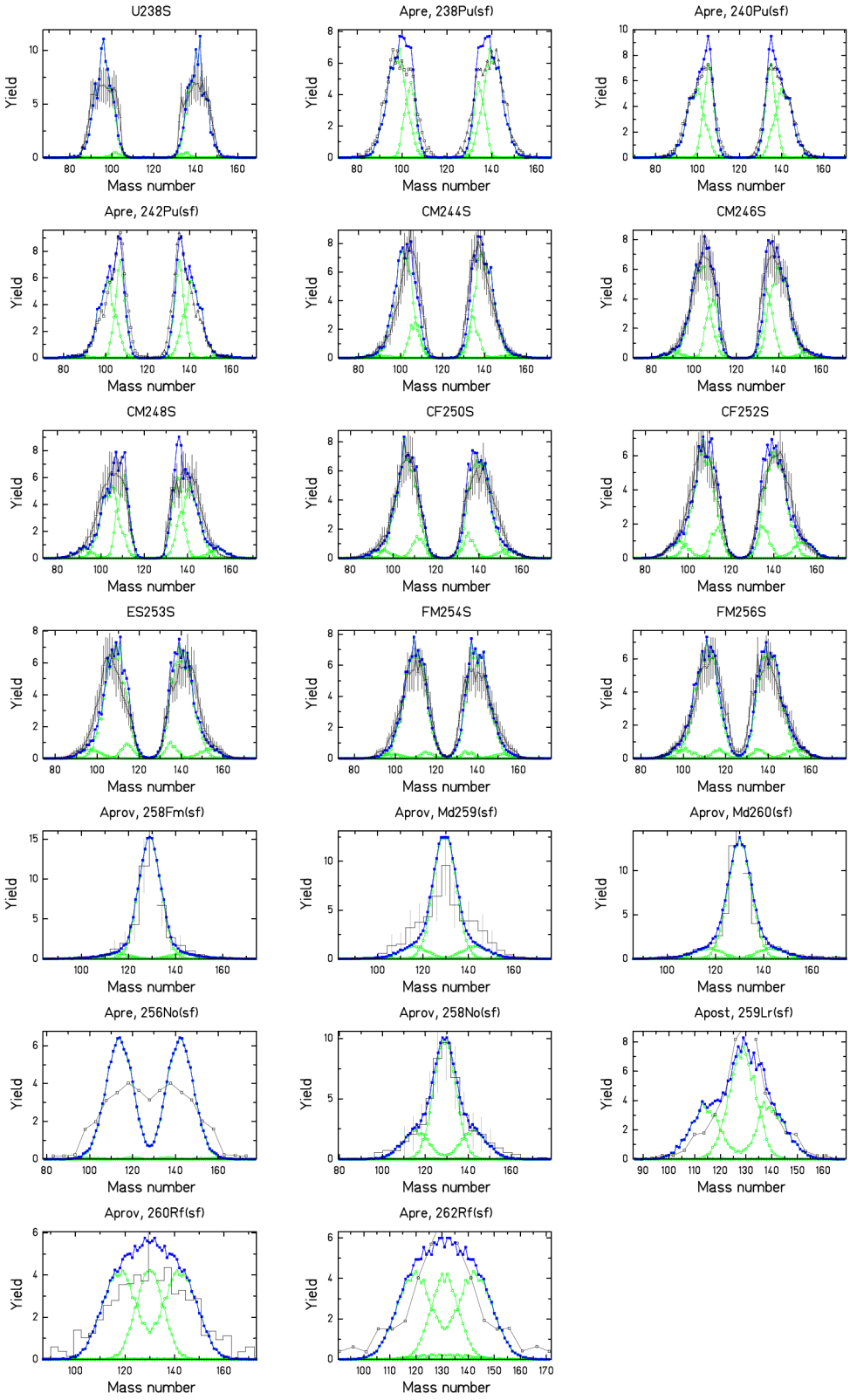

Figure 3: Same as figure 2, but with linear scale.

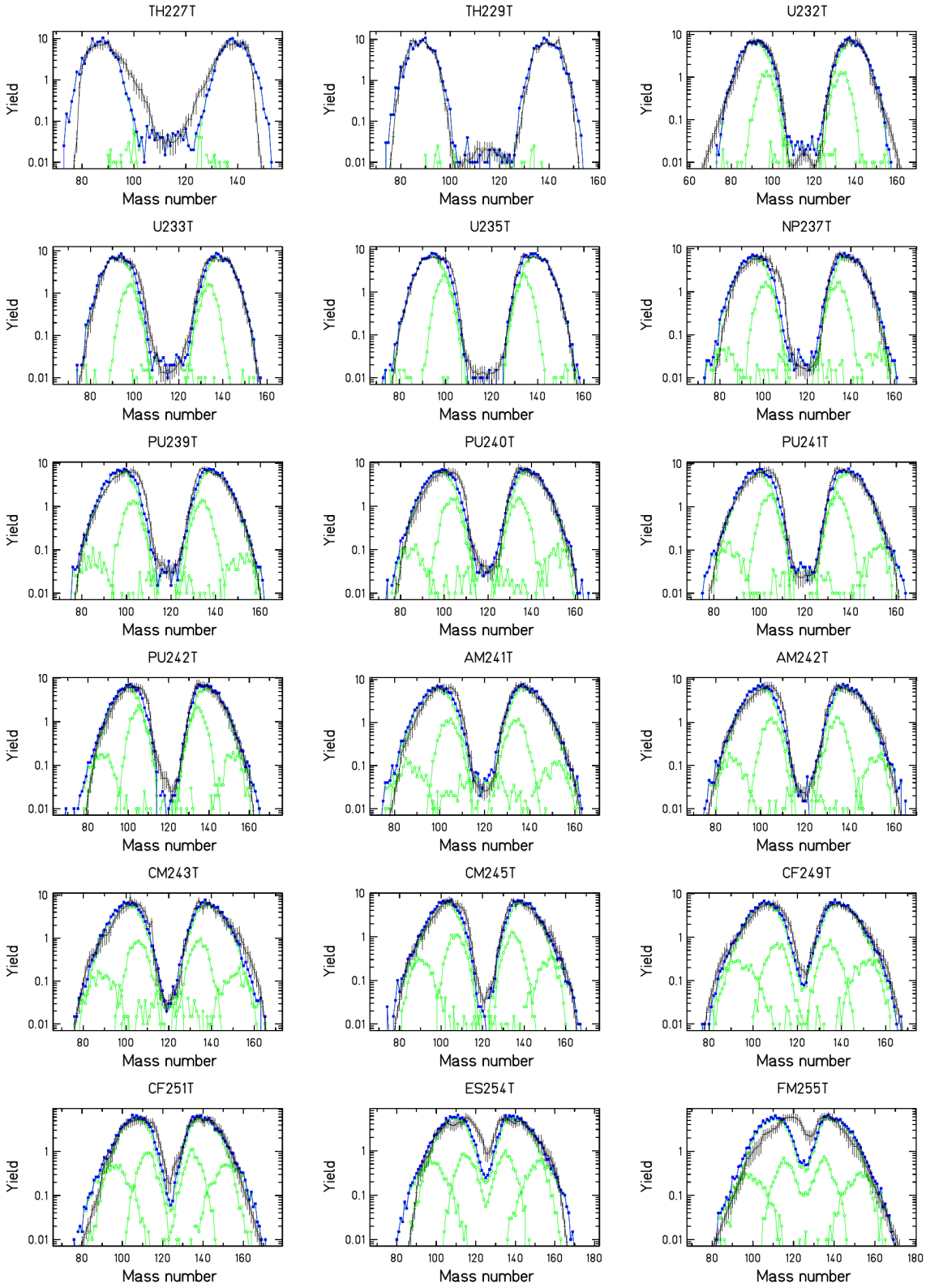

Figure 4: Comparison of experimental and evaluated post-neutron mass distributions (n_{th},f) [59] (crosses) with results of the model [58] (full symbols). The contributions of the different fission channels are shown in addition (open symbols). The target nuclei are indicated.

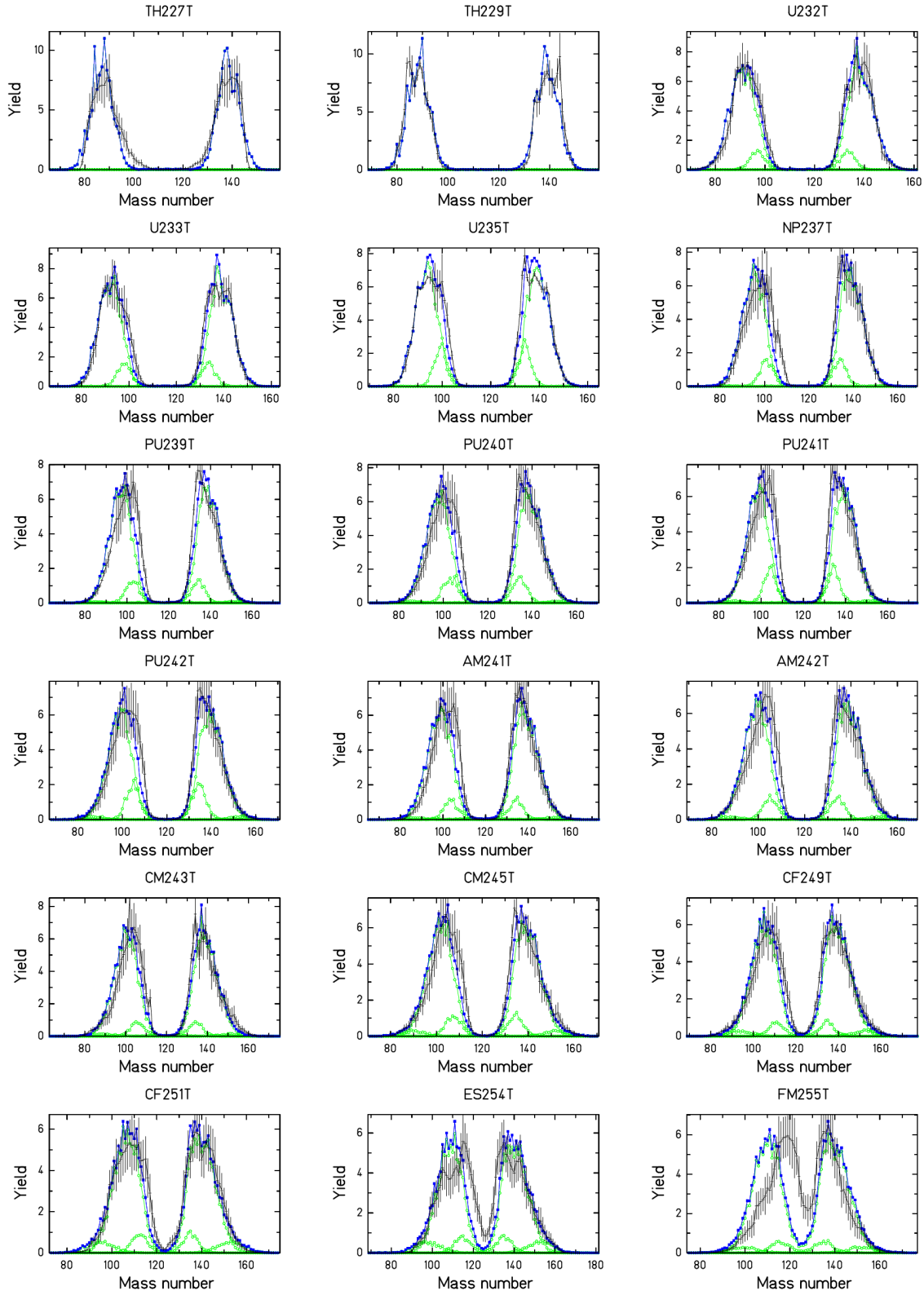

Figure 5: Same as figure 4, but with linear scale.

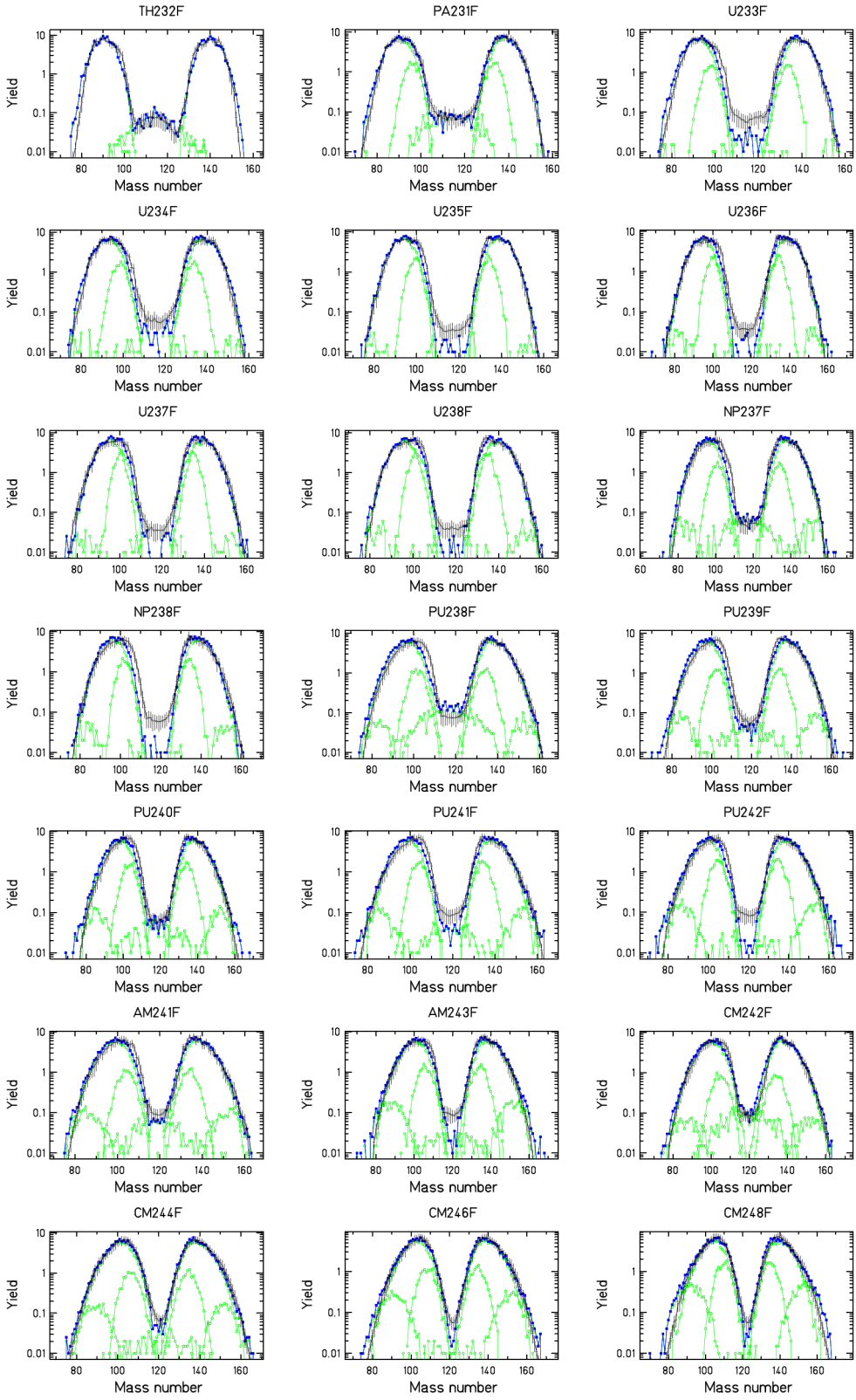

Figure 6: Comparison of evaluated post-neutron mass distributions from fast-neutron-induced fission (n,f) [59] (crosses) with results of the model [58] (full symbols). The contributions of the different fission channels are shown in addition (open symbols). The target nuclei are indicated

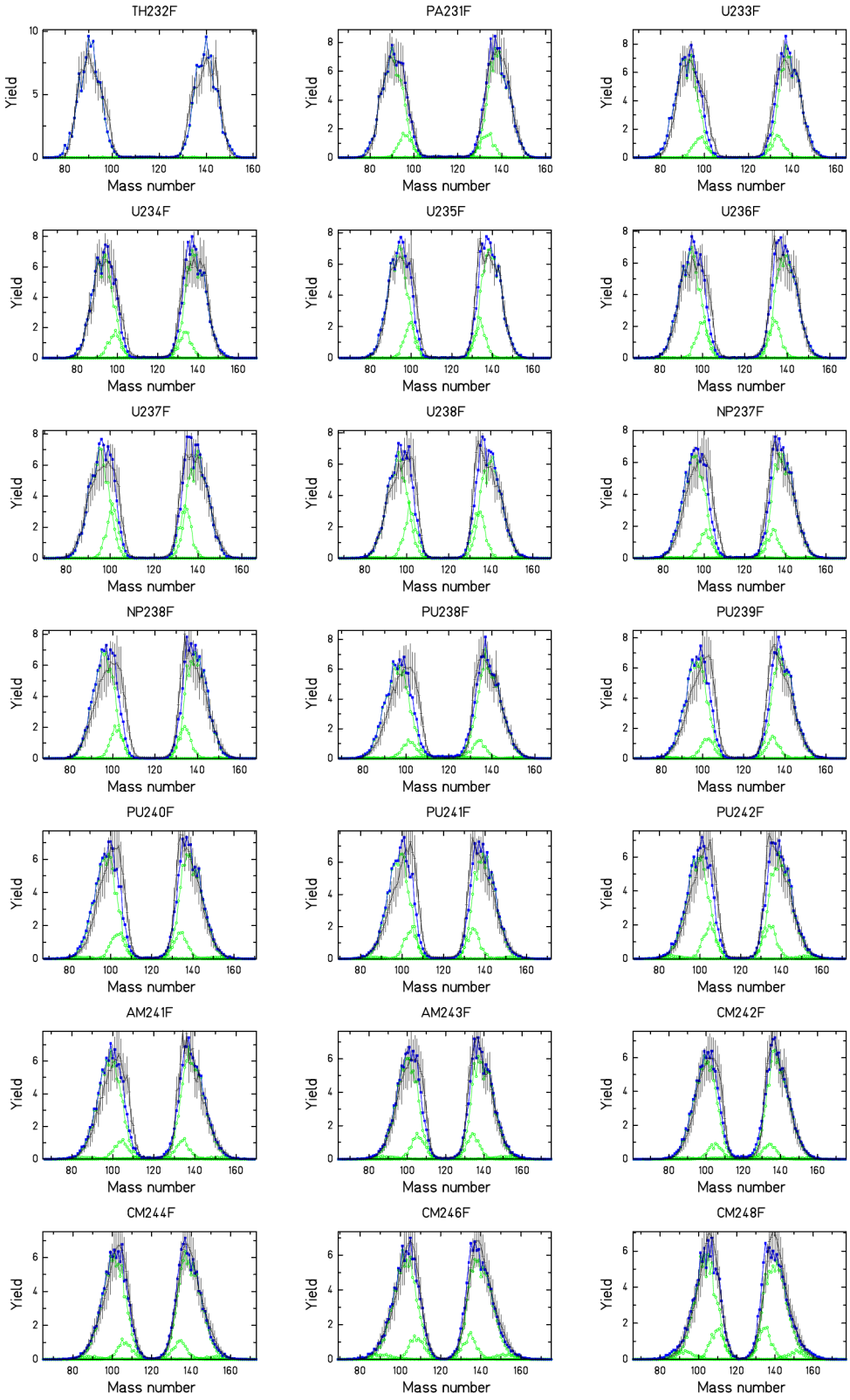

Figure 7: Same as figure 6, but with linear scale.

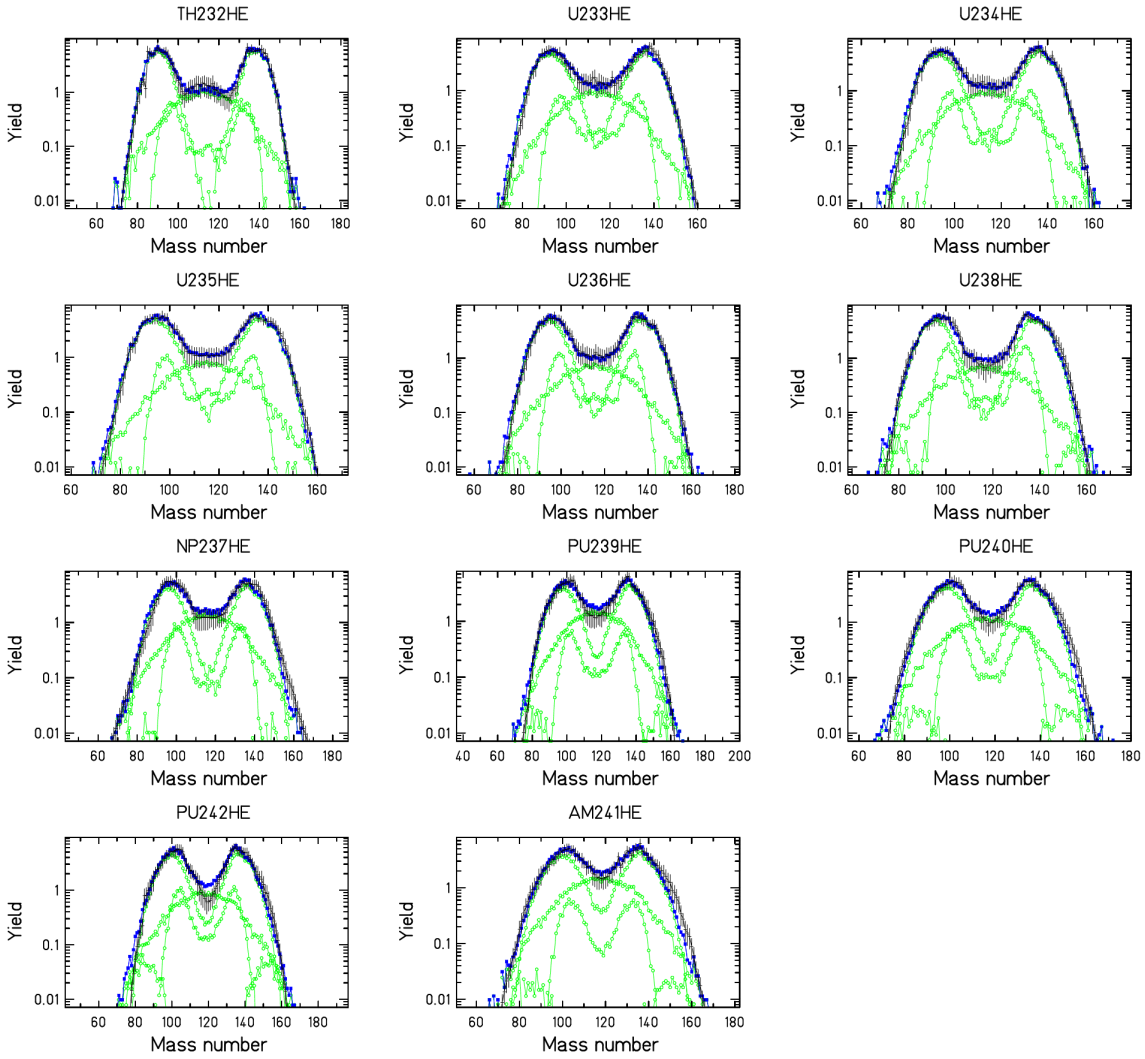

Figure 8: Comparison of evaluated post-neutron mass distributions from 14.7 MeV-neutron-induced fission (n,f) [59] (crosses) with results of the model [58] (full symbols). The contributions of the different fission channels are shown in addition (open symbols). The contributions from the different fission chances are deduced from the extrapolation of the empirical energy dependence of the first-chance fission probability. The target nuclei are indicated.

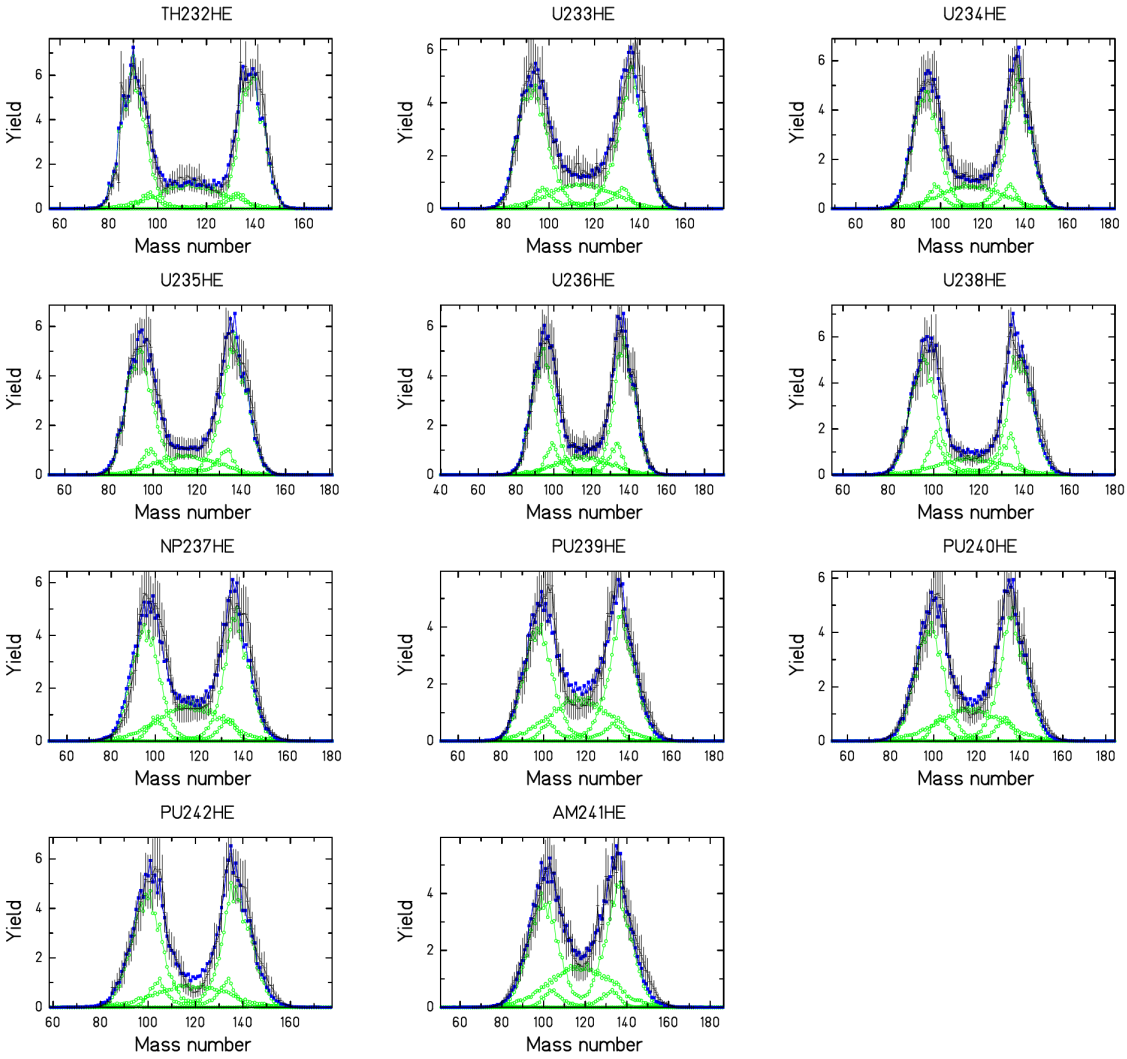

Figure 9: Same as figure 8, but with linear scale.

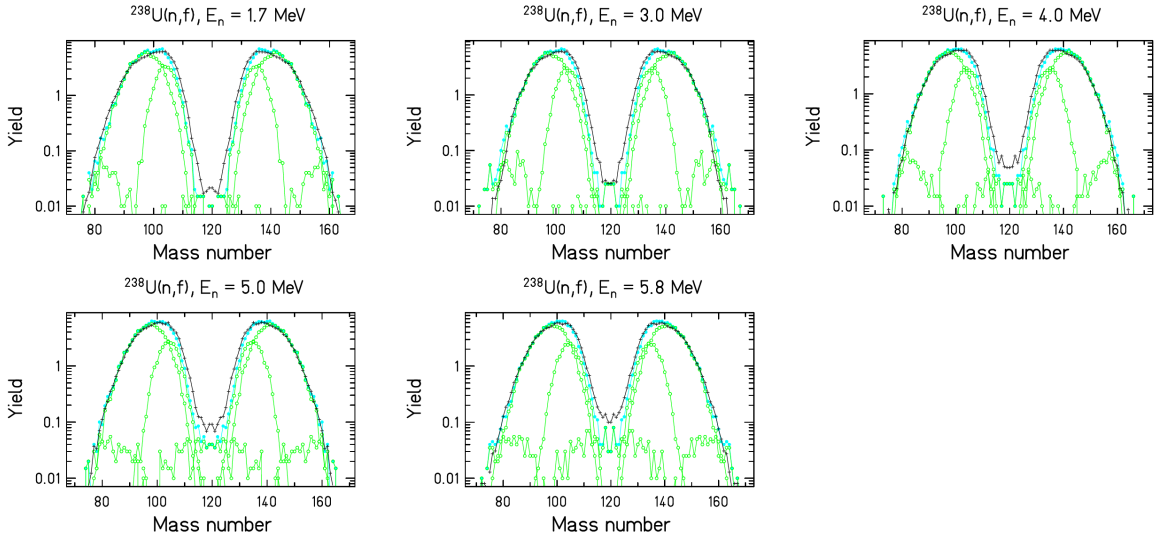

Figure 10: Measured pre-neutron mass distributions from neutron-induced fission of ^{238}U [62] in comparison with the results of the GEF code [58]. The neutron energies are indicated.

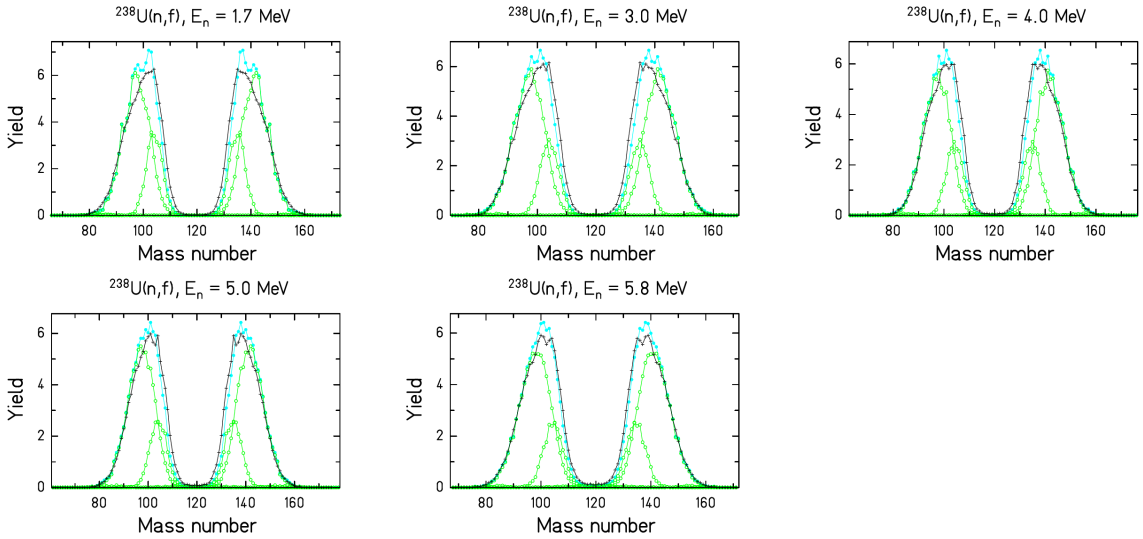

Figure 11: Same as figure 10 but with linear scale.

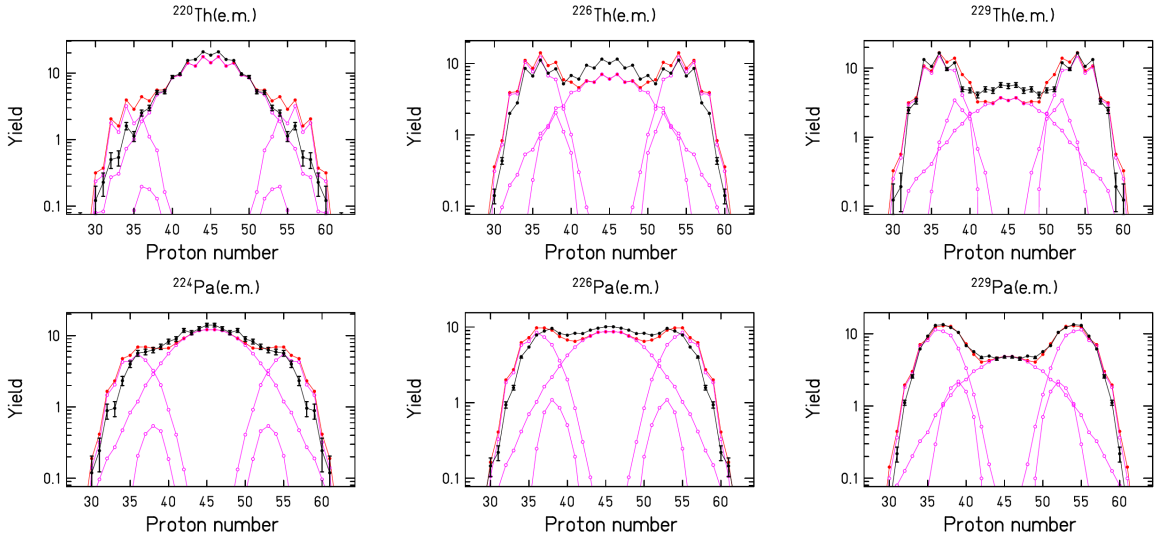

Figure 12: Fission-fragment nuclear-charge distributions. The measured data from electromagnetic-induced fission (ref. [30]) are compared with the results of the GEF code [58].

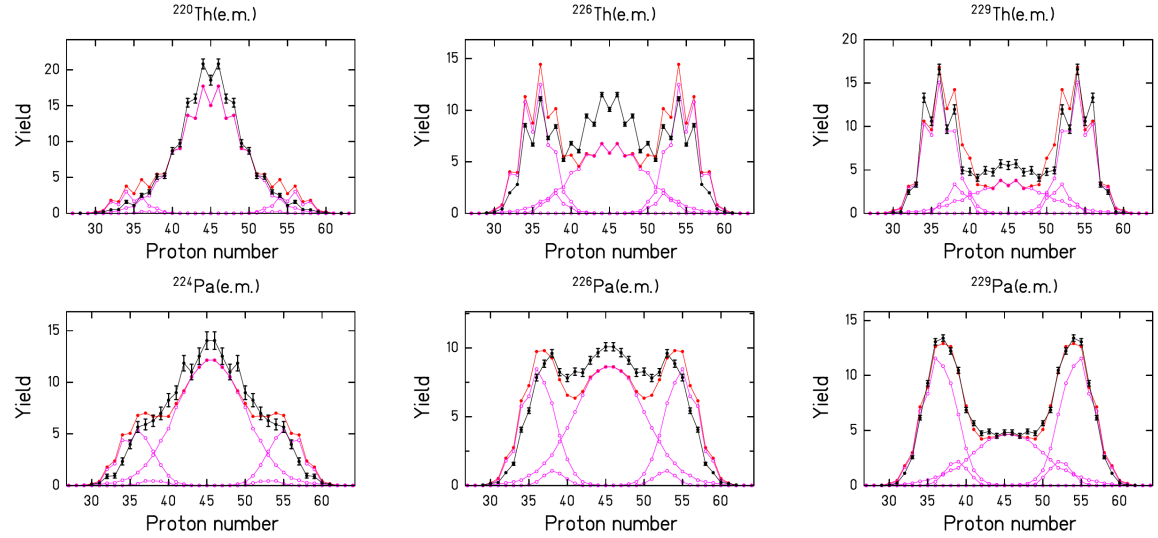

Figure 13: Same as figure 12, but with linear scale.

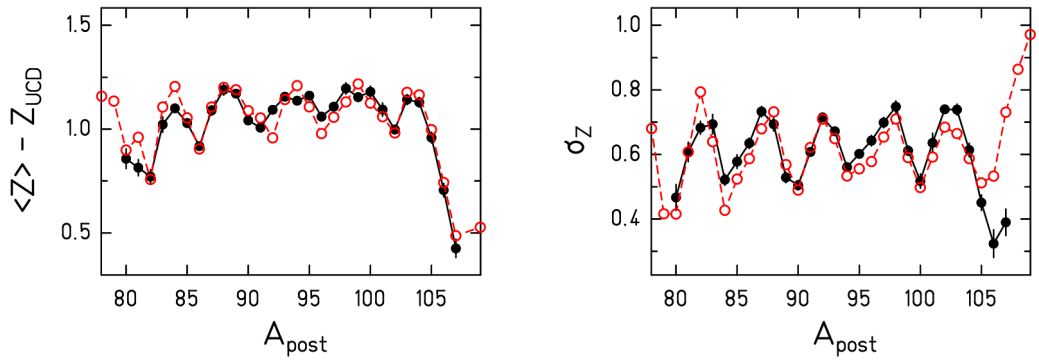

Figure 14: Charge polarisation (left) and widths of isobaric charge distributions (right) for the reaction $^{235}U(n_{th},f)$. The data from ref. [63] (full symbols) are compared with the result of the GEF code [58].

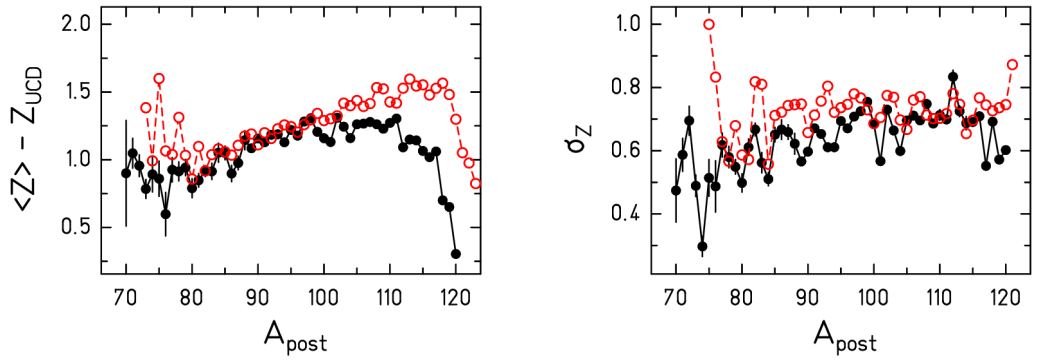

Figure 15: Charge polarisation (left) and widths of isobaric charge distributions (right) for the reaction $^{249}Cf(n_{th},f)$. The data from ref. [64] (full symbols) are compared with the result of the GEF code [58].

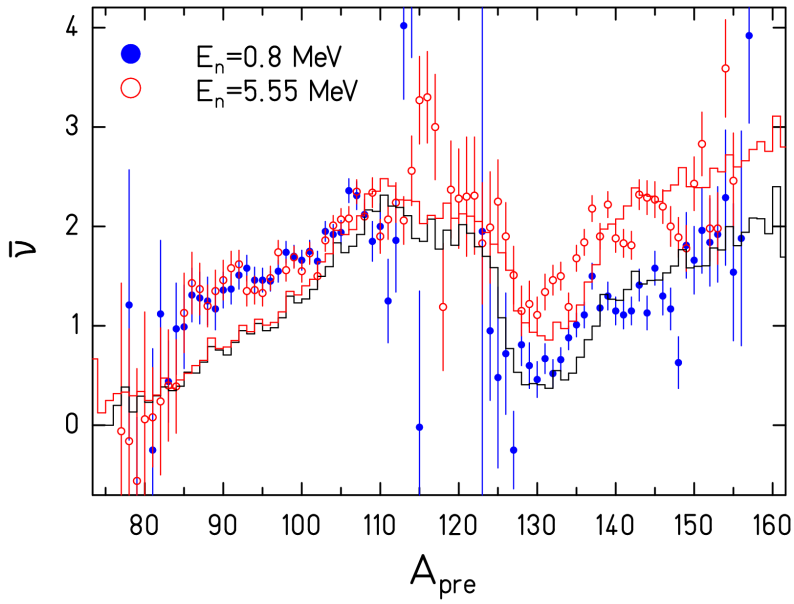

Figure 16: Mean number of prompt fission neutrons as a function of the pre-neutron fragment mass for neutron-induced fission of ^{237}Np. The energy values of the incident neutrons are indicated. The data [65] (points) are compared with the result of the GEF code (histogram).

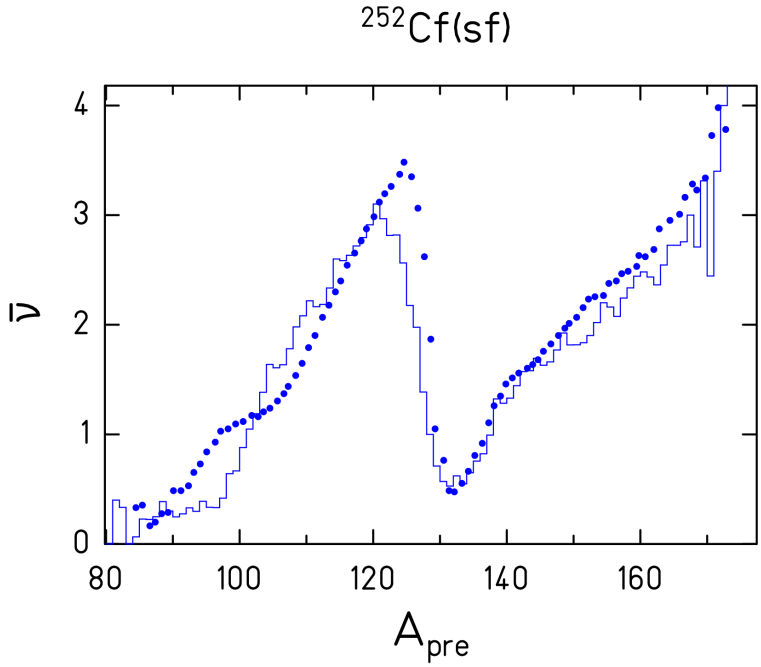

Figure 17: Mean number of prompt fission neutrons as a function of the pre-neutron fragment mass for spontaneous fission of ^{252}Cf. The data [66] (points) are compared with the result of the GEF code (histogram).

In the following, we will investigate the most important deviations, which show up when the experimental and evaluated data are confronted with the results of the GEF code. In particular, we will try to find the origin of the problems. Some systematic deviations have already been removed by including some additional effects in the code in an empirical manner, since either the theoretical explanation or a quantitative description were not in reach.

6.1 Relative weight of symmetric fission

We observed some deviations in the relative weight of the symmetric fission channel, which vary, in most cases gradually, from system to system. We suppose that they originate from weak shells in the fragments. These shells are not strong enough to generate a specific fission channel, but they may modulate the yields as shown in ref. [29]. Since the positions of the symmetric mode in neutron and proton numbers depend on the fissioning system, the shell effect at symmetry might slightly vary. Rather small shell effects in the order of a few 100 keV can explain these deviations.

Whenever the available data allowed, the additional shell effect of the symmetric fission channel was determined and added in an empirical table to the GEF code. In the calculated mass distributions shown in Figs. 2 to 11, these corrections are inlcuded. When this information is not available, the relative weight of the symmetric channel is subject to a larger uncertainty.

6.2 Charge polarisation

We noticed that the charge polarisation as predicted by the macroscopic scission-point model is not able to reproduce the measured values of the SL and the S2 fission channels. Therefore, we applied an additional shift of the isobaric charge distribution in the GEF code (see table 1). This problem had already been noticed previously [19]. It remains unclear, whether an increase of the neck parameter *d* as suggested in ref. [19] can solve this problem.

6.3 Trans-fermium nuclei

The description of the drastic changes of the mass distributions from one nucleus to another in the region of the heaviest nuclei are very delicate. In addition, the experimental conditions for measuring the mass distributions for these nuclei are very difficult, and therefore the uncertainties may be rather important. These difficulties should be considered when judging the discrepancies found in the mass distribution of ^{256}No(sf) (Figs. 2 and 3).

6.4 Possible deficiencies in the evaluated data for ^{227}Th(n_{th},f), ^{254}Es(n_{th},f), and ^{255}Fm(n_{th},f)

There are a few cases, where it seems possible that the evaluated files have some deficiencies.

The evaluated mass distribution for ^{227}Th(n_{th},f) (Figs. 4 and 5) shows tails at the inner side of the asymmetric components towards mass symmetry. These tails are in sharp contrast to result of the model calculation. Since the result of the model is in nice agreement with the data of all neighbouring nuclei, it seems possible that these tails are an artifact of the evaluation.

Another kind of discrepancy appears in the mass distributions of ^{254}Es(n_{th},f) and ^{255}Fm(n_{th},f). There is a shift of the position of the minimum near symmetry. The position of the minimum is obviously related to the prompt-neutron yield. From the mean value of the evaluated mass distributions, one can deduce a prompt neutron yield of 2.08 for ^{255}Fm(n_{th},f). From the experimental values of about 4 and 3.9, for spontaneous fission of ^{254}Fm and ^{256}Fm, respectively [67], one would have expected a prompt neutron yield of about 4.5 for ^{255}Fm(n_{th},f). Thus, it seems obvious that there is a problem in the evaluation: The prompt neutron yield is severely underestimated.

6.5 Position of the light mass peak

In many cases one observes a slight displacement of the position of the light mass peak to lower masses in the results of the code if compared to the data, probably caused by an overestimated number of prompt neutrons in this mass region. This problem is obviously a deficiency of the model, which might be cured by a better adjustment of the model parameters.

6.6 S3 fission channel

There are many cases, where some discrepancies show up between evaluated mass distributions and the result of the GEF code in the region of the S3 fission channel. The origin of this problem may be related to the low yield of this channel. As a consequence, the experimental mass yields in this far-asymmetric region have large uncertainties. These make it difficult to fix the parameters of the S3 fission channel in the code. In addition, the scarce data may also be responsible for some deficiencies of the evaluated data.

6.7 Charge polarisation of $^{249}Cf(n_{th},f)$

The charge polarisation in $^{249}Cf(n_{th},f)$ shows a drastic discrepancy between mass 100 and symmetry, see figure 15. After a careful investigation of this problem we suppose that the experimental data in this region are not correct. This conclusion is based on two facts: First, the model calculation reproduces the measured independent yields in the complementary heavy fragments very well. Secondly, the data in question have been obtained under difficult experimental conditions, because the *Z* resolution in this experiment was very poor in the heavy wing of the light fragment group.

Conclusions

A new fission model has been developed. It is based on the statistical population of states in the fission valleys at the moment of dynamical freeze-out, which is specific to each collective degree of freedom. Three fission channels are considered. The separability principle governs the interplay of macroscopic and microscopic effects. The newly discovered energy-sorting mechanism determines the division of intrinsic excitation energy between the fragments at scission and the creation of a strong even-odd effect at large mass asymmetry. This model gives a new insight into several dynamical times.

The model provides a consistent description of the fission observables from polonium to rutherfordium, from spontaneous fission to initial excitation energies up to about 20 MeV, with the same parameter set. (Note, however, that the GEF code calculates only first-chance fission. The energy dependent fission probabilities, which are needed in the case of multi-chance fission must be provided independently.) Most parameters are fixed from independent sources, only about 20 parameters have specifically been adjusted. Since the parameters of the model are closely related to physical properties of the systems, valuable conclusions on the fission process can be deduced. The good reproduction of measured data and the high predictive power of the code make it useful for applications in nuclear technology and complement the use of purely empirical models.

Acknowledgements

This work was performed during several short-term visits of K.-H. S. at the CENBG, financed by the EURATOM 6. Framework Programme "European Facilities for Nuclear Data Measurements" (EFNUDAT), contract number FP6-036434. K.-H. S. also thanks the CENBG for warm hospitality. Kilian Kern, KIT Karlsruhe, shared with us his observations when benchmarking the GEF code.

1 U. Brosa, S. Grossmann, and A. Mueller, Phys. Rep. **197**, 167 (1990).
2 A. C. Wahl, Atom. Data Nucl. Data Tables **39**, 1 (1988).
3 P. Moeller et al., Nature **409**, 785 (2001).
4 M. C. Duijvestijn et al., Phys. Rev. C **64**, 014607 (2001).
5 H. Goutte et al., Phys. Rev. C **71**, 024316 (2005).
6 D. Lunney et al., Rev. Mod. Phys. **75**, 1021 (2003).
7 I. O. Morales et al., Nucl. Phys. A **828**, 113 (2009).
8 V. M. Strutinsky, Nucl. Phys. A **122**, 1 (1968).
9 P. Moeller and J. R. Nix, Nucl. Phys. A **536**, 20 (1992).
10 M. Goeppert-Mayer, Phys. Rev. **75**, 1969 (1949).
11 D. Haxel et al., Phys. Rev. **75**, 1766 (1949).
12 W. D. Myers and W. J. Swiatecki, Nucl. Phys. A **612**, 249 (1997).
13 M. Goeppert-Mayer, Phys. Rev. **78**, 16 (1950).
14 D. Haxel et al., Z. Phys. **128**, 295 (1950).
15 C. Samanta and S. Adhikari, Phys. Rev. C **65**, 037301 (2002).
16 P. Moeller et al., Phys. Rev. C **79**, 064304 (2009).
17 M. G. Itkis et al., Z. Phys. A **320**, 433 (1985).
18 J. Benlliure et al., Nucl. Phys. A **628**, 458 (1998).
19 B. D. Wilkins et al., Phys. Rev. C **14**, 1832 (1976).
20 S. I. Mulgin et al., Phys. Lett. B **462**, 29 (1999).
21 F. J. Hambsch et al., Nucl. Data for Science and Technology, Conf. Proc., vol 59, SIF, Bologna, 1997, p. 1239.
22 A. V. Karpov et al., Phys. Rev. C **63**, 054610 (2001).
23 A. V. Karpov and G. D Adeev, Eur. Phys. J. A **14**, 169 (2002).
24 K.-H. Schmidt et al., Europh. Lett. **83**, 32001 (2008).
25 U. Mosel and H. W. Schmitt, Nucl. Phys. A **165**, 73 (1971).
26 Scientific report STI/PUB/1286 (IAEA, Vienna, 2008) ISBN 92-0-115306-6.
27 N. Bohr and J. A. Wheeler, Phys. Rev. **56**, 426 (1939).
28 P. N. Nadtochy and G. D. Adeev, Phys. Rev. C **72**, 054608 (2005).
29 S. I. Mulgin et al., Nucl. Phys. A **640**, 375 (1998).
30 K.-H. Schmidt et al., Nucl. Phys. A **665**, 221 (2000).
31 J. P. Unik et al., Proc. Symp. Phys. Chem. Fission, IAEA vol. 2, 19 (1974).
32 Yu. Oganessian, J. Phys. G: Nucl. Part. Phys.**34**, R165 (2007).
33 C. Boeckstiegel et al., Nucl. Phys. A **802**, 12 (2008).
34 K.-H. Schmidt and B. Jurado, Phys. Rev. Lett. **104**, 212501 (2010).
35 K.-H. Schmidt and B. Jurado, arXiv:1007.0741v1 [nucl-th] (2010).
36 A. Gilbert and A. G. W. Cameron, Can. J. Phys. **43**, 1446 (1965).
37 T. von Egidy et al., Phys. Rev. C **72**, 044311 (2005).
38 M. Guttormsen et al., Phys. Rev. C **68**, 034311 (2003).
39 A. V. Voinov et al., Phys. Rev. C **79**, 031301 (2009).
40 H. A. Bethe, Phys. Rev. 50, **332** (1939).
41 M. G. Itkis et al., Phys. Atom. Nucl. **58**, 2026 (1995).
42 J. R. Nix, Nucl. Phys. A **130**, 241 (1969).
43 A.Ya. Rusanov et al., Yad. Fiz. **60**, 773 (1997).
44 V. V. Pashkevich, Nucl. Phys. A **169**, 275 (1971).
45 I. Ragnarsson and R. K. Sheline, Phys. Scr. **29**, 385 (1984).
46 IAEA TECDOC-1168 (IAEA, Viena 2000).
47 U. Brosa et al., Phys. Rev. **59**, 767 (1999).
48 H. Naik et al., J. Phys. G: Nucl. Part. Phys. **30**, 107 (2004).
49 U. Brosa et al., Phys. Rev. C **59**, 767 (1999).
50 M. G. Mustafa et al., Phys. Rev. C **7**, 1519 (1973).
51 U. Mosel and H. Schmitt, Phys. Rev. C **4**, 2185 (1971).
52 J. Maruhn and W. Greiner, Z. Phys. **251**, 211 (1972).
53 H. J. Krappe and S. Fadeev, Nucl. Phys. A **690**, 431 (2002).
54 M. Asghar and R. W. Hasse, J. Phys. Colloques **45**, C6-455 (1984).
55 K.-H. Schmidt and B. Jurado, arXiv:1010.0917v1 [nucl-th] (2010).
56 M. Caamano et al., arXiv:0909.1059v2 [nucl-ex] (2010).
57 F. Rejmund et al., Nucl. Phys. A **678**, 215 (2000).
58 The GEF code and additional information are available from www.cenbg.in2p3.fr/GEF
59 M. B. Chadwick et al., Nucl. Data Sheets **107**, 2931 (2006).
60 L. Dematte et al., Nucl. Phys. A **617**, 331 (1997).
61 D. C. Hoffman, M. R. Lane, Rad. Acta **70/71**, 135 (1995).
62 F. Vives et al., Nucl. Phys. A **662**, 63 (2000).
63 W. Lang et al., Nucl. Phys. A **345**, 34 (1980).

64 M. Djebara et al., Nucl. Phys. A **496**, 346 (1989).
65 A. A. Naqvi et al., Phys. Rev. C **34**, 218 (1986).
66 A. C. Wahl, Atom. Data Nucl. Data Tables **39**, 1 (1988).
67 D. C. Hoffman and M. M. Hoffman, Ann. Rev. Nucl. Sci. **24**, 151 (1974).